Evidence for nonzero electron velocity at the tunnel exit in strong-field atomic ionization



(Received 12 February 2024; accepted 27 March 2024; published 15 April 2024)

We provide some evidence for nonzero electron velocity at the tunnel exit in strong-field atomic ionization. Our investigation is based on the analysis of a suitably chosen correlation function which describes correlations between the two observables: the longitudinal electron velocity and the appearance of the photoelectron in the continuum at the end of the laser pulse. The results of the correlation function analysis that we perform are confirmed by the calculations using the quantum orbits method.

DOI: 10.1103/PhysRevResearch.6.023049

I. INTRODUCTION

Electron tunneling induced by a strong laser field is a fundamental process, which underpins a range of important technological innovations such as high-order harmonic generation [1], photoelectron holography [2], and creation of metastable atomic states [3]. When the tunneling occurs in a slow varying laser field, the photoelectron leaves the tunnel adiabatically with a zero velocity in the direction of the laser field [4]. The adiabatic tunneling constitutes the basis of the so-called simple man model (SMM) [5,6]. In this model it is assumed that the electron emerges into the continuum with zero longitudinal velocity and its subsequent motion is guided by the the laser field alone.

When variation of the laser field is fast, the tunneling occurs nonadiabatically and the photoelectron can leave the tunnel with a nonzero longitudinal velocity [7]. This effect has been studied in the literature, see, e.g., Refs. [8,9]. Recently, nonadiabatic tunneling received considerable attention in the context of attosecond angular streaking, the experimental technique also known as the attoclock [10–12]. Nonadiabatic tunneling affects significantly interpretation of the attoclock measurements [13,14], see also recent reviews on the attoclock technique [15–18].

Experimental studies of nonadiabatic tunneling employ various laser field configurations. The attoclock technique

Published by the American Physical Society under the terms of the Creative Commons Attribution 4.0 International license. Further distribution of this work must maintain attribution to the author(s) and the published article's title, journal citation, and DOI.

is based on close-to-circular [10–12] or bicircular [19,20] laser fields. Similar studies can be conducted with elliptical [21–23] or counter-rotating two-color linear fields [24,25]. Photoelectron holography can also be employed to probe the longitudinal momentum at the tunnel exit [26]. In many of these studies, a nonzero longitudinal velocity is inferred by comparing the experimental results with the classical trajectory Monte Carlo (CTMC) simulations [18,27–29]. While this comparison is convincing, it lacks the direct access to the photoelectron velocity at the tunnel exit. Closer insight is provided by more advanced theoretical approaches [30–33].

In the present work, we offer a very direct and graphical evidence of nonzero tunneling velocity. In our study we employ the correlation analysis of strong field atomic ionization developed in our preceding works [34-37]. This analysis is based on suitably constructed two-time correlation functions that serve particular needs. In Ref. [35] we used this technique to study lateral velocity distribution in strong field ionization process. This approach allowed us to study time evolution of the lateral velocity distribution for the ionized electron during the interval of the laser pulse duration. We found that for the case of the short range Yukawa potential, this evolution follows closely the scenario obtained in the framework of the well-known strong field approximation (SFA) method [4,7,38–40], which stipulates that this distribution is a Gaussian with the parameters which undergo little change after the moment of ionization. A completely different behavior was found in the case of the Coulomb potential. The lateral velocity distribution in this case was observed to have Gaussian shape only for the times near the moment of ionization, subsequent temporal evolution resulting in development of the cusp in the distribution. This cusp is a well-known feature of the lateral velocity distribution for ionization of the Coulombic systems [41]. Our approach allowed us to study the process of temporal development of

In the present application, we use the correlation analysis to isolate the continuous part of the photoelectron wave packet

^{*}igorivanov@ibs.re.kr

[†]A.Kheifets@anu.edu.au

[‡]schimmoller.11@buckeyemail.osu.edu

[§]landsman.7@osu.edu

^{||}kyungtaec@gist.ac.kr

and to study evolution of the longitudinal component of the electron velocity during the ionization process.

II. METHOD

Our approach allows us to overcome one of the main difficulties in studying temporal development of the ionization process. The very notion of the ionization event or the ionized electron is not very easy to formulate in the framework of the conventional quantum mechanics (QM). The physical reason for that is quite simple, for the times inside the laser pulse, when the wave packet describing ionized electron has not left the atom, it is difficult to unambiguously separate the part of the wave function describing ionized electron from the total wave-function of the system. The well-known SFA and Perelomov-Popov-Terent'ev (PPT) methods [4,7,38–40,42] introduce such a separation by representing the solution of the time-dependent Schrödinger equation (TDSE) in the integral form using the Dyson equation and dropping out the term corresponding to the unperturbed atomic wave function [43]. Such a strategy, though offering great insight, is not entirely rigorous, the separation of the parts of the wave function done this way depends on the gauge used to describe atom-field interaction. This fact is responsible for the lack of the gauge invariance of the SFA or PPT approaches [43].

We use an alternative approach. It is based on the fact that the wave packets corresponding to the ionized and the nonionized parts of the wave function become well separated after the end of the laser pulse. We formulate, therefore, the questions about temporal behavior of different observables in the following way: what would be the probability of detecting a given value of the observable inside the laser pulse, provided that the electron is found in the ionized state at the end of the laser pulse. The question, formulated in this way, looks like classical conditional probability problem. There is, however, a difference with the classical probability theory. Indeed, the notion of the conditional probability cannot be unambiguously formulated in quantum mechanics [44–46]. We can, however, use the next best thing, a correlation function characterizing correlation between the two observables at different moments of time. Such a correlation function can be naturally defined using the Heisenberg representation.

III. FORMALISM

We write the correlation function between the observables *A* and *B* in the following form:

$$C(A(t_1)B(t_2)) = \langle \phi_0 | \hat{A}^H(t_1) \hat{B}^H(t_2) | \phi_0 \rangle$$

= $\langle \hat{A}\Psi(t_1) | \hat{U}(t_1, t_2) \hat{B}\Psi(t_2) \rangle$. (1)

Here the operators $\hat{A}^H(t)$ and $\hat{B}^H(t)$ corresponding to the observables A and B are taken in the Heisenberg representation, $|\phi_0\rangle$ is the initial state of the system. For the purpose of a practical calculation we use a more familiar Schrödinger form given in the second line of Eq. (1), where $\Psi(t)$ is the time-dependent Schrödinger wave function describing an atom in the laser field, and $\hat{U}(t,0)$ is the evolution operator driving the quantum evolution of the system, so that $\Psi(t) = \hat{U}(t,0)\phi_0$.

We have shown that by choosing for $\hat{B}^H(t)$ the Heisenberg form of a suitable Schrödinger projection operator describing

the final electron state one can study the dynamical development of ionization processes [35,36] or frustrated tunneling ionization [37]. The reason why this approach works can be understood readily from the Schrödinger form in the second line of Eq. (1). Let us choose in this formula $\hat{B} = \hat{P}$, where \hat{P} is the projection operator on the continuous spectrum of the field-free atomic Hamiltonian, and $t_2 = T_1$, where T_1 is the moment of time when the laser pulse is gone. According to the well-known projection postulate of the QM [47], the vector $|\hat{P}\Psi(t_2)\rangle$ represents, apart from an unimportant normalization factor, the state of the system immediately after the measurement that has found the electron in an ionized state.

In the present application, we define the observable A in Eq. (1) by means of the projection operator:

$$\hat{P}_{v_{\tau}} = |\phi_{v_{\tau}}\rangle\langle\phi_{v_{\tau}}|, \qquad (2)$$

where the components of the ket vector $|\phi_{v_z}\rangle$ in the momentum representation are

$$\phi_{v_z}(\mathbf{p}) = \langle \mathbf{p} | \phi_{v_z} \rangle = N e^{-a^2 (\mathbf{p} - \mathbf{e}_z v_z)^2} . \tag{3}$$

Here N is a normalization factor and the parameter a defines the resolution with which we look at the evolution of the ionized electron in the momentum space. In all the calculations that we report below, we employ the length gauge and, therefore, we need not make a distinction between the electron momentum and velocity.

The correlation function (1) with thus defined observables A and B specifies a quantum-mechanical amplitude of finding an electron in the state $|\hat{P}_{v_z}\Psi(t_1)\rangle$, with the momentum space wave function peaking around the value e_zv_z at the moment $t=t_1$, on the condition that the electron is found in the ionized state after the end of the pulse. It offers, therefore, an opportunity to track evolution of the ionized electron velocity for times inside the laser pulse. In the calculations below, we used the value a=8.3, which allows us to probe the ionized electron velocity with the resolution of approximately 0.1 a.u.

Practical numerical calculation of the correlation function (3) necessitates multiple solutions of the TDSE. For this purpose we employed a TDSE solver tested in our previous works [48–50]. The calculation is a relatively straightforward, albeit computationally demanding procedure, which follows the steps we described in detail in the previous works [34–37].

All the calculations reported below have been performed with a linearly polarized Gaussian pulse. The electric field of the pulse $E(t) = -\partial A(t)/\partial t$ is defined in terms of the vector potential:

$$\mathbf{A}(t) = -\hat{\mathbf{e}}_z \frac{E_0}{\omega} e^{-\alpha \zeta^2} \sin(\omega t) , \qquad (4)$$

where $\zeta = t - T/2$, $T = 2\pi/\omega$ is an optical cycle (o.c.) corresponding to the base frequency ω . The majority of the calculations reported below were performed for the base frequency $\omega = 0.057$ a.u. (the wavelength of 800 nm). We employ the value $\alpha = 0.0076$ in the Eq. (4), which corresponds to the pulse intensity full width at half maximum of 175 as. The electric field and vector potential of the pulse thus defined are shown in Fig. 1. Similar single oscillation pulses with circular polarization were used in numerical attoclock simulations [51–54]. Even though such pulses are hard to

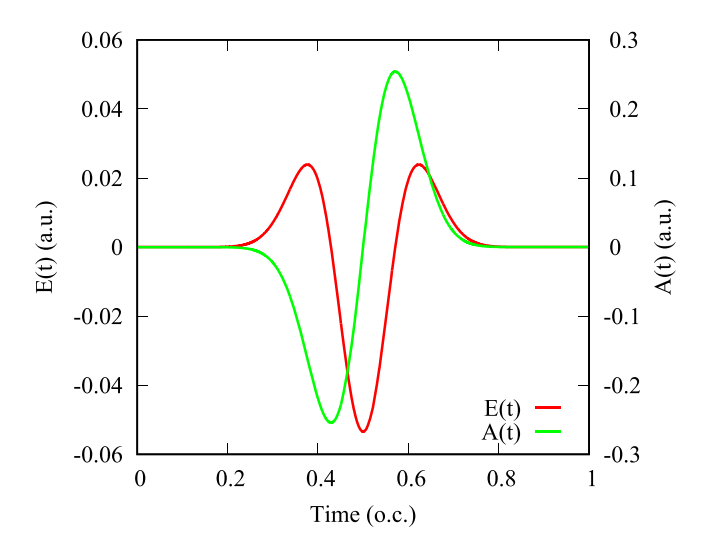


FIG. 1. Electric field of the pulse.

realize experimentally, they provide a greater transparency in interpreting theoretical results.

In the present application, the use of an ultrashort laser pulse gives us the following advantages. First, it allows us to concentrate below on the contributions of only three main maxima of the electric field of the pulse, located correspondingly at $t=0.377\,\mathrm{T}$, $t=0.5\,\mathrm{T}$, and $t=0.623\,\mathrm{T}$. Second, for the pulse (4) with the parameter α specified above, the values of E(0) and E(T) are of the order of 10^{-11} a.u., which allowed us to restrict the soluti on of the TDSE describing evolution of the system to the interval (0,T) to diminish the computational cost.

IV. RESULTS

Using the tools and computational strategies described above we perform a correlation analysis of tunneling ionization of various target atoms at different laser pulse strengths. Our results are exhibited in Figs. 2–5 where we display the absolute value of the correlation function. As we mentioned above, apart from an overall normalization factor, the

correlation function we study can be related to the quantum-mechanical amplitude of finding an electron localized in the velocity space near particular value v_z at the moment t inside the laser pulse, on the additional condition that the electron is found in the ionized state after the end of the pulse. Thus constructed correlated function provides us, therefore, with the means to follow the ionized electron trajectory in the velocity space as the ionization process develops.

The trajectories obtained as a result of the quantum calculation can be compared with the classical trajectories we obtained by performing CTMC simulations. In doing these simulations we used the standard prescription of the CTMC calculations [27,28]. The classical trajectories were launched at the local field maxima with the corresponding initial values for the spatial coordinates defined by the feld direction model [28]. Initial values for the velocities in the CTMC calculations were chosen to better reproduce the location of the maxima of the correlation function patterns. We impose an additional condition on the initial velocities in these simulations restricted by the symmetry of the pulse, requiring that the initial velocities for the CTMC trajectories launched at the secondary maxima (t = 0.377 T and t = 0.623 T) of the pulse be equal.

We start our analysis with the model Yukawa atom bound by the short-range potential $V(r) = -1.903e^{-r}/r$ and having the ionization potential of 0.5 a.u. The absolute value of the correlation function for the Yukawa atom is displayed in Fig. 2 for two different field strengths. The patterns displayed in both panels of Fig. 2 can be easily understood using the SMM. Within this model, electron emerges into the continuum with zero velocity. The longitudinal velocity of an electron ionized at a particular moment t_0 inside the pulse is therefore given at a later time t by the difference of the vector potentials $A(t) - A(t_0)$. If we concentrate on the electrons emitted at the local maxima of the pulse where $A(t_0)$ is near zero, as shown in Fig. 1, we can expect the electron velocity to mimic closely the vector potential A(t) of the pulse. This is indeed precisely what Fig. 2 exhibits. Black dashed lines in the figure show the vector of the pulse. One can see that the correlation pattern indeed follows very closely the vector potential as the SMM suggests. The dashed white, yellow, and cyan lines

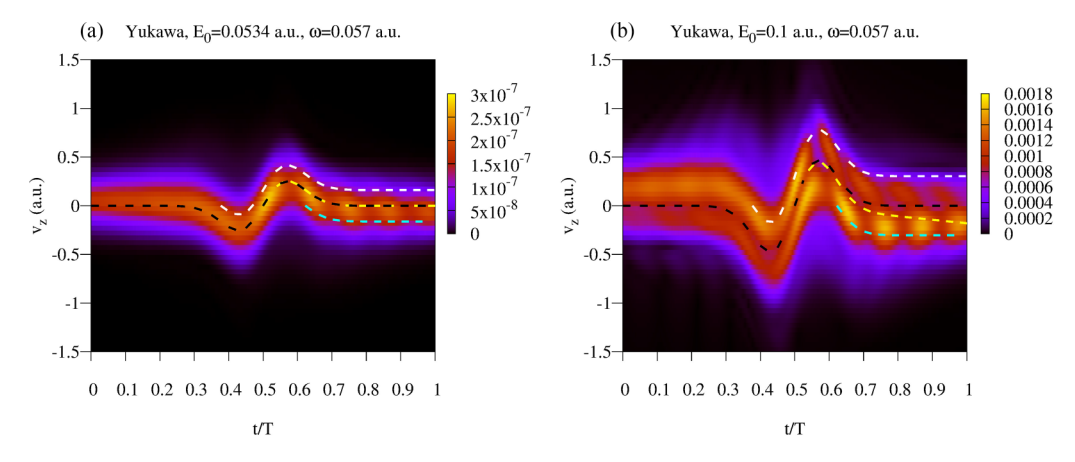


FIG. 2. Absolute values of the correlation function for electron velocity for Yukawa atom. Dashed lines in the plots show the CTMC trajectories for the electrons launched at the local maxima of the electric field at t = 0.377 T (white), t = 0.5 T (yellow), and t = 0.623 T (cyan), respectively, and the vector potential of the pulse (black).

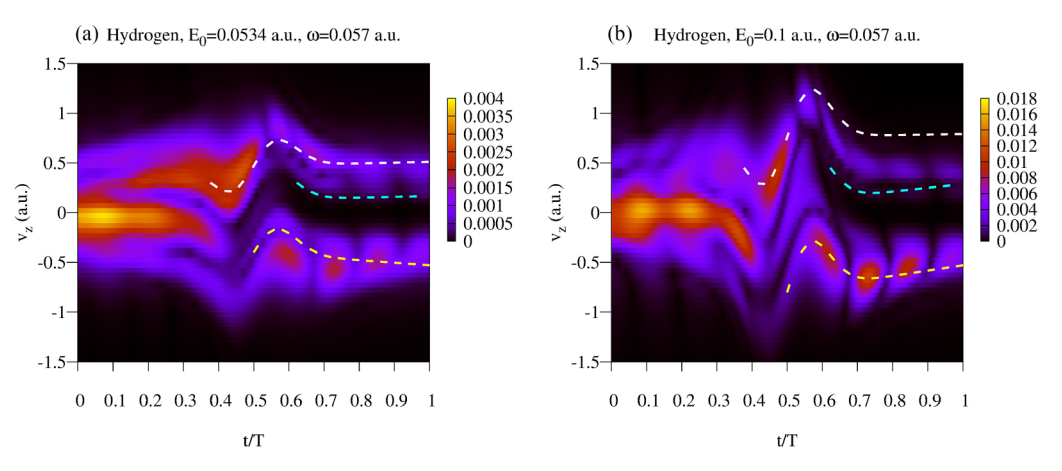


FIG. 3. Absolute values of the correlation function for the electron velocity for hydrogen. Dashed lines in the plots show the CTMC trajectories for the electrons launched at the local maxima of the electric field at $t = 0.377 \,\text{T}$ (white), $t = 0.5 \,\text{T}$ (yellow), and $t = 0.623 \,\text{T}$ (cyan), respectively.

visualize the classical trajectories for the electrons launched at the three local maxima of the electric field at $t=0.377\,\mathrm{T}$, $t=0.5\,\mathrm{T}$, and $t=0.623\,\mathrm{T}$, respectively. The initial velocities in the CTMC simulation were chosen, as described above, to make the trajectories follow as closely as possible the location of the maxima of the correlation function pattern. As can be seen from Table I, these velocities are very close to zero.

We expand our analysis further to real atoms in which the departing photoelectron experiences the Coulomb drag of the parent ion. The correlation analysis results are presented in Figs. 3–6 for the hydrogen, helium, and argon atoms at different pulse strengths and base frequencies. Ionization from the helium and argon atoms is described within the single active electron (SAE) approximation with the effective potentials provided in Ref. [55]. Unlike the short-range Yukawa potential, these potentials have a long-range Coulomb tail. We see that the ionization scenario visualized in Figs. 3–6 is different from the one for the short-range Yukawa atom. In no way can the classical CTMC trajectories launched at the field maxima with zero velocities describe adequately the evolution of the correlation function. We had to use nonzero initial velocities in the CTMC simulations to achieve a reasonably

good agreement between the pictures provided by the CTMC and the correlation function approaches. The corresponding velocities v_z are listed in Table I.

We see that for the pure Coulombic case of hydrogen the sign and the magnitude of v_z correspond to the parameters of the electric field at the instant of tunneling. As the peak field strength E_0 increases, the magnitude of the initial v_z value grows accordingly. For the helium and argon targets this is not necessarily the case. In particular, for the case of the main field maximum at t=T/2, initial v_z values are practically the same for both targets and both field strengths shown in Table I. This shows that detailed form of the atomic potential certainly influences initial velocity which electron acquires at the moment of ionization.

In the picture based on the SFA, electron velocity at the instant of ionization is determined by the so-called sub-barrier stage of the electron motion, when electron travels under the barrier created by the ionic and external electric fields. This motion can be studied in detail using the quantum orbits method [56]. Quantum orbit is a (generally complex) trajectory which describes under-the-barrier motion of the ionized electron. Before discussing results of the calculations using

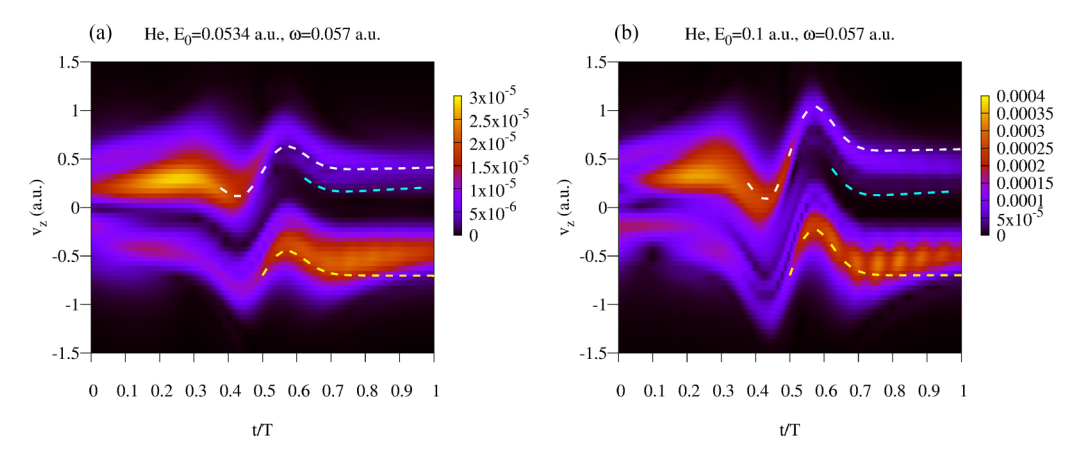


FIG. 4. Absolute values of the correlation function for electron velocity for helium. Dashed lines in the plots show the CTMC trajectories for the electrons launched at the local maxima of the electric field at $t = 0.377 \,\text{T}$ (white), $t = 0.5 \,\text{T}$ (yellow), and $t = 0.623 \,\text{T}$ (cyan), respectively.

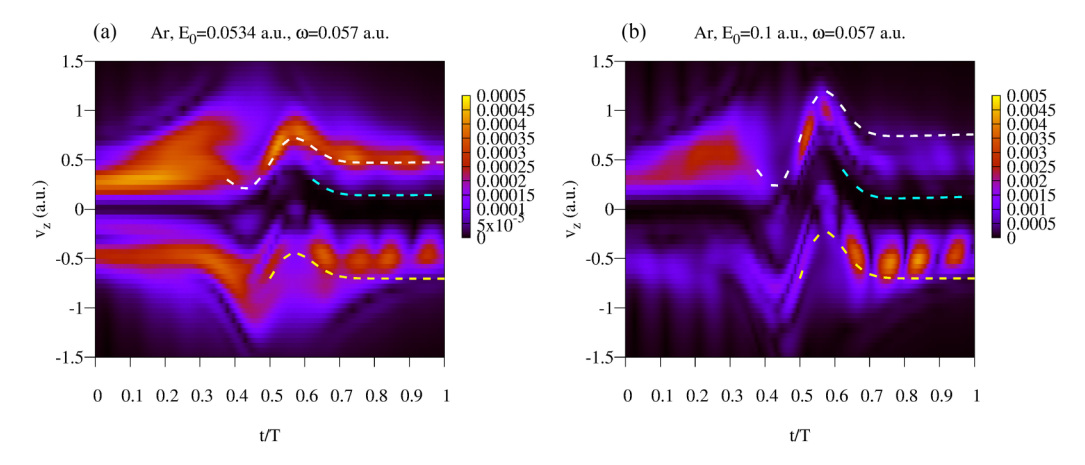


FIG. 5. Absolute values of the correlation function for electron velocity for argon. Dashed lines in the plots show the CTMC trajectories for the electrons launched at the local maxima of the electric field at t = 0.377 T (white), t = 0.5 T (yellow), and t = 0.623 T (cyan), respectively.

this method in the next section, we will present first a few general remarks of a qualitative character, which might elucidate the role of the shape of the atomic potential in producing nonzero initial v_z .

For helium and argon atoms, the potential of the ionic field assumes its asymptotic Coulomb form -1/r at the distances $r > r_a$, where $r_a \sim 1$ a.u. is the approximate size of the atom. The tunnel exit point, on the other hand, is located at the distance $r_{\rm ex} \approx I_p/E_0$ [43], where I_p is the target ionization potential, and E_0 is the peak electric field strength. For the field strengths and the helium and argon targets that we consider $r_{\rm ex} \sim 10$ a.u., therefore, on the major part of the sub-barrier motion, the electron is effectively driven by the -1/r Coulomb potential. The role of the detailed shape of the atomic potential in determining the value of the initial v_z consists, therefore, not so much in its effect on the electron motion outside the atom, as in setting initial conditions for the sub-barrier electron trajectory. The most probable trajectories are those for which electron's velocity and coordinates are real at the tunnel exit [43]. To produce such a trajectory, suitable initial conditions determining subsequent motion have to be chosen. These conditions are imposed inside the atom, so their choice is affected by the detailed form of the ionic potential at small distances from the ionic core. It is through this mechanism that the shape of the ionic potential at small distances affects the magnitude of the initial v_z . This may explain the difference in the initial longitudinal velocities patterns for hydrogen on one hand, and helium and argon, on the other.

For the lower frequency case of $\omega = 0.02$ a.u., shown in Fig. 6(b) the correlation pattern follows the pulse vector potential markedly more closely than for $\omega = 0.057$ [Fig. 6(a)]. This is an expected behavior, of course, for the nonadiabatic effects are weaker for low frequencies.

V. DISCUSSION

A. Role of the Coulomb potential

Figures 3–6 and Table I show that the initial electron velocities are of the same order of magnitude for the hydrogen, helium, and argon atom and are practically zero for the Yukawa atom. It is, therefore, the Coulomb potential that, most likely, is responsible for producing nonzero initial v_z . To support this conjecture, and to elucidate the role of the Coulomb potential, we performed a series of additional calculations.

We consider first a soft core Coulomb potential $V(r) = -\frac{1.3}{\sqrt{r^2 + 0.4}}$ whose parameters are chosen so that ionization potential of this system is 0.5 a.u. The results of this additional simulation are shown in Fig. 7. It reveals that the initial electron velocities are very similar to that of the hydrogen atom exhibited in Fig. 3. This result shows that the non-Coulombic character of the potential at small distances plays a relatively minor role in producing the nonzero initial values for v_z . The shape of the potential at larger distances, in particular the Coulomb tail, is probably more important.

TABLE I. Initial velocities v_z (a.u.) at the local field maxima in various targets at different field strengths.

	Peak field strength E_0 , a.u.							
	0.0534	0.1	0.0534	0.1	0.0534	0.1	0.0534	0.1
t/T	Yukawa		Hydrogen		Helium		Argon	
0.377	0.005	0.006	0.302	0.442	0.197	0.251	0.299	0.391
0.500	-0.001	0.006	-0.384	-0.796	-0.694	-0.685	-0.696	-0.695
0.623	0.005	0.006	0.302	0.442	0.197	0.251	0.299	0.391

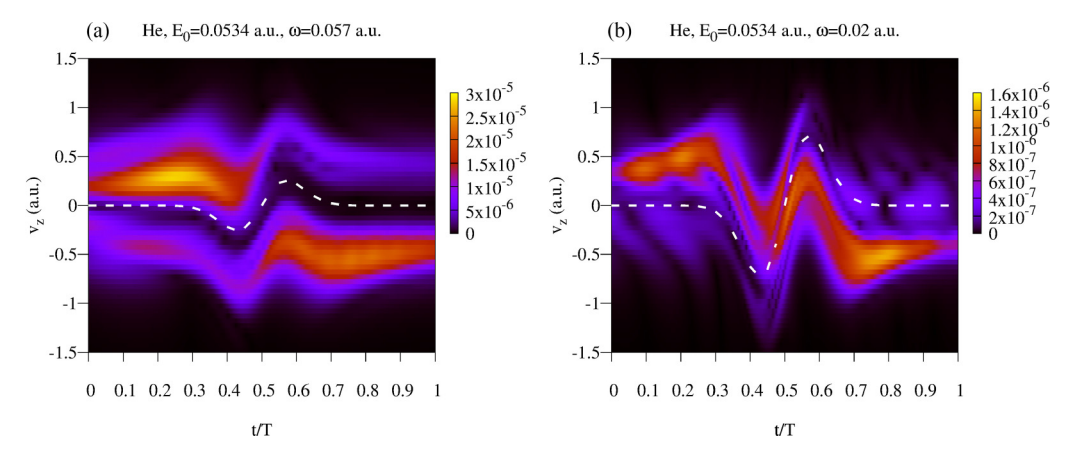


FIG. 6. Absolute values of the correlation function for electron velocity for helium for different base frequencies of the laser field. White dashed lines show the vector potential of the pulse.

To elucidate the Coulomb tail effect we performed a series of calculations using a cutoff Coulomb potential $V(r) = -\frac{f(r)}{r}$, where

$$f(r) = 1, \quad r < r_0,$$

$$f(r) = 3(r_0 + 1 - r)^2 - 2(r_0 + 1 - r)^3, \quad r_0 \leqslant r \leqslant r_0 + 1,$$

$$f(r) = 0, \quad r > r_0 + 1.$$
 (5)

The potential defined in Eq. (5) is Coulombic for $r < r_0$, being switched off smoothly in the interval $(r_0, r_0 + 1)$. Results of the calculations for different values of the cutoff parameter r_0 are presented in Fig. 8. As we can see, the correlation patterns shrink in vertical direction with decreasing r_0 , until for $r_0 = 3$ a.u. we practically recover the curve mimicking the vector potential which we saw in Fig. 2(a) for the short- range Yukawa potential. Thus, we confirm that the long-range Coulomb tail extending to sufficiently large distances from the center is a necessary prerequisite for a nonzero initial longitudinal velocity of the tunneling electron. This statement requires certain qualifications to be made more accurately. What matters, we believe, is not the presence of the Coulomb tail per se at very large distances from the ionic core. To be more precise, we should say that results shown in Fig. 8 indicate that to have the nonzero initial longitudinal velocity we should require the potential to be Coulombic on a major part of the interval of the sub-barrier electron motion.

B. Quantum orbits

We can have a further glimpse at how this velocity develops by examining the quantum mechanical amplitude of the tunneling process. Clearly, the nonzero initial velocity may appear only during the sub-barrier motion of the electron. Within the framework of the SFA and the saddle point method (SPM), this stage of the ionization process is described as a motion in imaginary time originating at the saddle point t_s [43]. The latter is a solution to the SPM equation:

$$(p + A(t_s))^2 + 2I_p = 0. (6)$$

The trajectory of the tunneling electron minimizes the semiclassical action

$$S(t_s, t, \mathbf{p}) = \int_{t_s}^{t} \left(\frac{(\mathbf{p} + \mathbf{A}(u))^2}{2} + I_p \right) du.$$
 (7)

In Eq. (7) p, A, and I_p are, respectively, the electron momentum, the field vector potential, and the target ionization potential. The path in the complex t plane describing the subbarrier motion is usually chosen as a segment of the straight line t_s , Re(t_s) descending from the saddle point t_s on the real

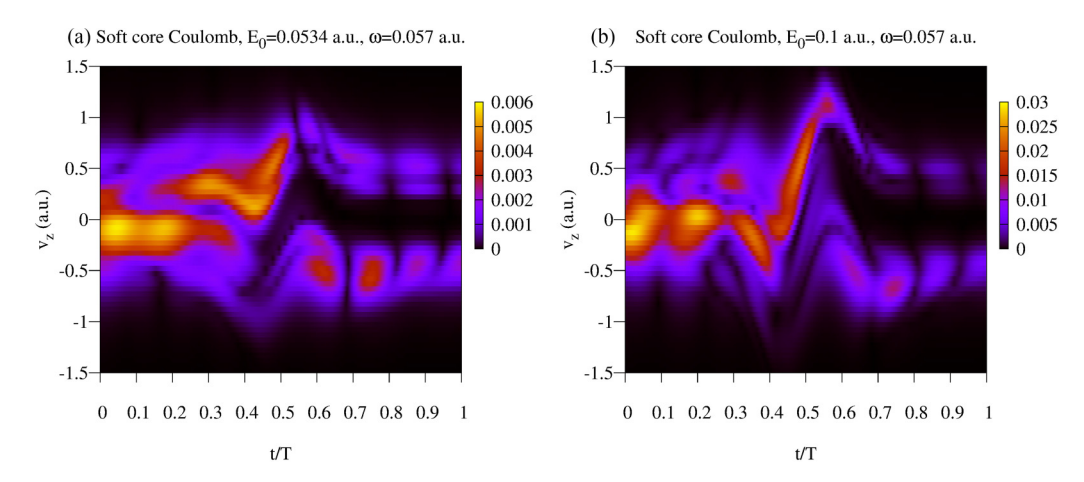


FIG. 7. Absolute values of the correlation function for electron velocity for the soft core Coulomb potential.

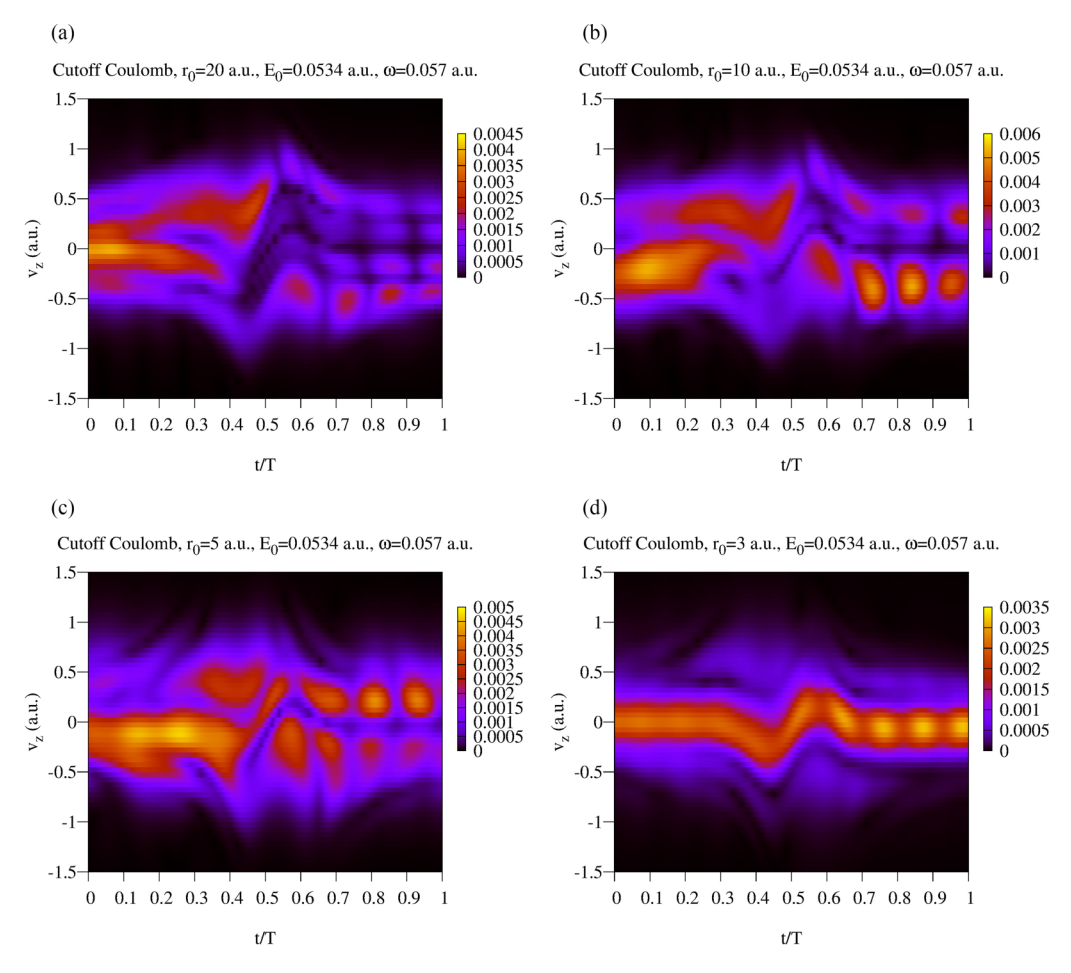


FIG. 8. Absolute values of the correlation function for electron velocity for the cutoff Coulomb potential.

time axis. Equation (7) is the key equation of the SFA, and it neglects completely effects of the atomic potential. In the SFA framework, the electron velocity along the path t_s , Re(t_s) is purely imaginary, which reflects the classical impossibility of the sub-barrier motion. At the moment $t = \text{Re}(t_s)$ which is interpreted as the moment of the tunnel exit, the longitudinal electron velocity is zero [43].

Effects of the atomic potential which might give a nonzero longitudinal electron velocity can be included using the quantum orbit analysis of the electron motion [56]. Unlike the SFA, which relies on the electron propagator neglecting the influence of the atomic potential, Lai *et al.* [56] employ the *ab initio* path integral representation of the electron propagator. Evaluation of the corresponding path integral leads to a modified saddle point equation:

$$(\mathbf{p}(t_s) + \mathbf{A}(t_s))^2 + 2I_p + 2V(\mathbf{r}(t_s)) = 0,$$
 (8)

which includes an atomic potential V(r).

The expression defining the action corresponding to the sub-barrier electron motion on the time interval (t_s, t_1) with $t_1 = \text{Re}(t_s)$ can be written as [56]

$$S(\mathbf{r}_1(t_1), \mathbf{v}_1(t_1), t_s) = I_p t_s - \int_{t_s}^{t_1} (\dot{\mathbf{p}}(t) \cdot \mathbf{r}(t) + \hat{H}(\mathbf{r}(t), \mathbf{p}(t), t))$$

$$\times dt, \qquad (9)$$

where

$$\hat{H}(\mathbf{r}(t), \mathbf{p}(t), t) = \frac{(\mathbf{p}(t) + \mathbf{A}(t))^2}{2} + V(\mathbf{r}(t))$$
(10)

is the Hamiltonian. In Eq. (9) v(t) = p(t) + A(t) and r(t) are electron velocity and coordinates on the sub-barrier interval of motion, V(r) is the atomic potential extended analytically to complex coordinate values.

We performed calculations for the soft core Coulomb potential with $V(r) = -\frac{1.3}{\sqrt{r}\cdot r + 0.4}$ and the soft core Yukawa potential with $V(r) = -\frac{3.45}{\sqrt{r}\cdot r + 0.4}e^{-\sqrt{r}\cdot r}$. The parameters of the potentials are chosen so that both systems have the ionization potential of 0.5 a.u. We chose the model atoms with the soft core potentials because the calculations in this case are somewhat easier to perform than for the hydrogen or Yukawa atoms, where the potentials have singularities for the real values of the coordinates.

Equations of motion corresponding to the Hamiltonian (10) are

$$\frac{d\mathbf{p}(t)}{dt} = -\nabla V(\mathbf{r}), \quad \frac{d\mathbf{r}(t)}{dt} = \mathbf{p}(t) + \mathbf{A}(t). \tag{11}$$

We solve these equations in the sub-barrier region of the electron motion using the following procedure. We pick a moment of time t_1 (the tunnel exit point) on the real axis and assume

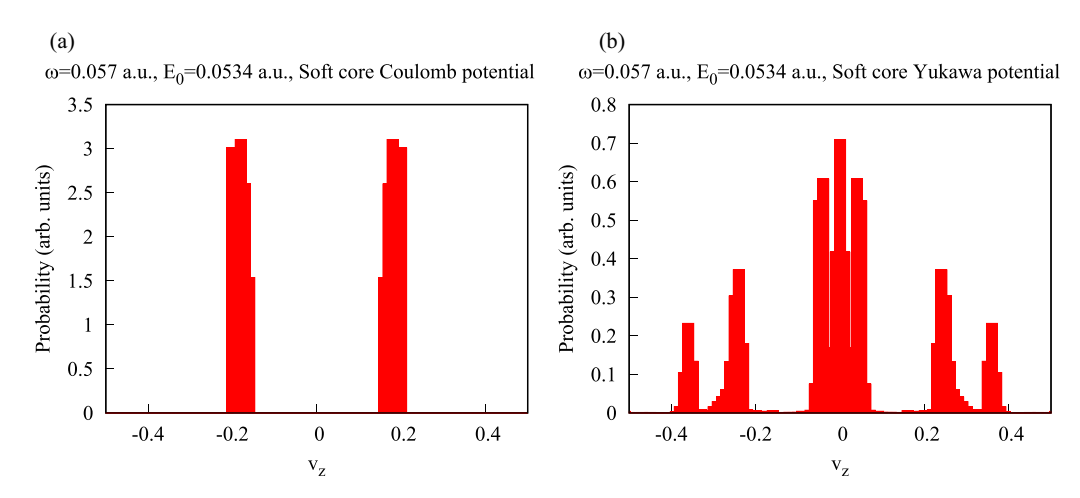


FIG. 9. Longitudinal velocity distributions obtained using Eq. (12) for the soft core Coulomb and Yukawa potentials.

that the electron coordinate $r(t_1)$ and velocity $v(t_1)$ at the tunnel exit are real. We then propagate the equations of motion (11) in time along the segment $(t_1, t_1 + i\tau)$ (with real positive τ) parallel to the imaginary time axis, verifying if the saddle point equation (8) is satisfied at any point along the trajectory. If such a point is found for a particular τ , we call the point $t_s = t_1 + i\tau$ the saddle point. Simultaneously, we compute the action (9) along the trajectory. This procedure is repeated for a grid of the exit times $t_1 \in (T/2 - T/10, T/2 + T/10)$ around the main maximum of the pulse (4), and grids of the real exit coordinates $r(t_1)$ and velocities $v(t_1)$. Because of the symmetry of the problem we need not solve the full 3D equations of motion (11), we have to solve only the two-dimensional version of these equations, assuming that the motion is confined to the (x, z) plane.

Thus we obtain the actions $S(\mathbf{r}(t_1), \mathbf{v}(t_1), t_s)$ describing the sub-barrier motion for the electron trajectories launched at various saddle points t_s , with various exit coordinates $\mathbf{r}(t_1)$ and velocities $\mathbf{v}(t_1)$ at the exit time $t_1 = \text{Re } t_s$.

Smaller values of the imaginary part of the action $S(\mathbf{r}(t_1), \mathbf{v}(t_1), t_s)$ correspond to more probable quantum trajectories, the relative weight of the trajectory being dampened by the factor $e^{-2\operatorname{Im} S}$ [56]. Imaginary part of action $S(\mathbf{r}(t_1), \mathbf{v}(t_1), t_s)$ provides us, therefore, with a probability measure for the quantum trajectories with different sets of exit parameters. Using this measure, we may define an (unnormalized) longitudinal velocity distribution:

$$P(v_z) = \sum_{r, v_x, t_s} \exp \{-2 \text{Im } S(r(t_1), v(t_1), t_s)\}.$$
 (12)

The sum in Eq. (12) includes all the quantum trajectories characterized by the set of parameters $\mathbf{r}(t_1)$, $\mathbf{v}(t_1)$, t_s , and $t_1 = \text{Re } t_s$, which we obtain using the algorithm we described above. One should bear in mind that expression (12) for the velocity probability distribution has only exponential accuracy and should be regarded as a semiclassical estimate.

The probability distributions (12) obtained for the soft core Coulomb and Yukawa potentials with the parameters we considered above are shown in Fig. 9.

The results in Figs. 3(a) and 7(a) show that the correlation patterns for the hydrogen atom and the model atom

with the soft core Coulomb potential are pretty similar. We can, therefore, make a direct comparison of the the results of the present quantum orbit calculation shown in Fig. 9(a) and the correlation pattern for the hydrogen atom in Fig. 3(a).

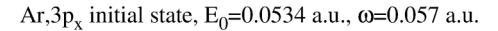
One can see from Fig. 9(a) that the distribution exhibits two symmetric maxima at the longitudinal velocities of approximately -0.18 a.u. and 0.18 a.u. The origin of this symmetric structure can be traced back to the structure of the equations of motion (11) and the saddle point equation (8). For the electric field E(t) of the pulse symmetric about the midpoint t = T/2 of the pulse on the real time axis, considered as an analytic function of time, the following equality holds: $E(-(t-T/2)^*) = E(t-T/2)^*$. It follows then, that since we start the sub-barrier propagation with real values of the coordinates and velocities at the real time axis, to every quantum orbit with the exit coordinates $r_1(T/2 + \Delta)$ and velocities $v(T/2 + \Delta)$ originating at the saddle point $T/2 + \Delta + i\tau_s$ with the real positive Δ and τ_s , corresponds a quantum orbit with the exit coordinates $r_1(T/2 - \Delta)$ and velocities $-v(T/2-\Delta)$ originating at the saddle point $T/2-\Delta+i\tau_s$. The actions (9) along these two quantum trajectories have the same imaginary parts, these trajectories are, therefore, equally probable.

The results obtained using the quantum orbits method are to be compared with the results obtained using the correlation function approach shown in Fig. 3(a). The quantum orbits analysis suggests that there should be two branches in the correlation pattern originating near the midpoint t = T/2 of the pulse. The positive velocities branch in the correlation pattern is more difficult to observe, however, as it is masked in the Fig. 3(a) by the band of the correlation pattern originating at the first field maximum. We do, however, observe a hint at the presence of such a structure for the positive velocities, which looks like a discontinuity of the correlation patterns in Figs. 3(a) and 3(b) near the midpoint t = T/2 of the pulse. The most probable value of the negative exit velocity as given by the quantum orbits method is approximately -0.18 a.u., which is in a relatively good agreement with the results shown in Fig. 3(a) and Table I for the hydrogen atom. The agreement is not perfect, which is probably due to the limited accuracy of the expression (12) that we noted above. More importantly, the general qualitative picture provided by the quantum orbits calculation which is shown in Fig. 9(a), confirms the presence of the nonzero longitudinal exit velocities in agreement with the results of the correlation function analysis.

Figure 9(b) shows results of the quantum orbit calculation for the soft core Yukawa potential. The distribution shown in Fig. 9(b) differs qualitatively from the soft core Coulomb results. It has a main maximum at zero velocity and a number of the weaker secondary maxima. Tentatively, we might attribute the presence of these maxima to the processes of multiple under-the-barrier reflections.

The presence of the main maxima at $v_z = 0$ is in agreement with the correlation pattern for the Yukawa potential shown in Fig. 2. It confirms thus the assertion we made above that the qualitative difference between the patterns shown in Fig. 2 and those shown in Figs. 3-5 is due to the presence of the Coulomb tail in the potential. Figure 2(a) does not show the secondary maxima which are present in the results of the quantum orbit calculation shown in Fig. 9(b). A possible explanation for this might be that with a limited resolution power in the velocity space which our approach provides, we do not resolve these maxima in the case of the field strength 0.0534 a.u. shown in Fig. 2(a). For the case of the higher field strength of 0.1 a.u. shown in Fig. 2(b), one can discern presence of a two-branch structure in the correlation pattern which could be interpreted as a manifestation of the secondary maxima with nonzero longitudinal velocities.

An interesting question is the role of the symmetry of the initial atomic state in forming the longitudinal velocity distribution. This role is quite important in the case of transverse velocity distribution, i.e., the velocity distribution in the directions perpendicular to the polarization vector [57]. The targets we considered above have initial states either of s symmetry (for the cases of the Yukawa, hydrogen, and helium atoms in Figs. 2-4) or p symmetry for the argon atom in Fig. 5. The results shown in Fig. 5 were obtained for the initial $3p_7$ state of the Ar atom, which in the SAE approximation we use was described by the wave function $R_{3p}(r)Y_1^0(\theta,\phi)$. Here $Y_l^m(\theta,\phi)$ is the spherical harmonic, and the radial wave function $R_{3p}(r)$ was obtained by solving the eigenvalue problem for the SAE Hamiltonian with the effective potential for an Ar atom [55]. We remind the reader that the electric field is polarized along the quantization z axis. By inspecting Figs. 2-5 one is tempted to conclude that the longitudinal velocity distribution is not affected significantly by the symmetry of the initial state wave function, the results for all the Coulombic systems shown in Figs. 3–5 being qualitatively similar. This conclusion is further supported by an additional calculation we perform for the Ar atom prepared initially in the $3p_x$ state, i.e., the state with the initial state wave function $R_{3p}(r)(Y_1^1(\theta,\phi)-Y_1^{-1}(\theta,\phi))$. The $3p_z$ and $3p_x$ states have the same energies, but different orientations, the $3p_z$ orbital is oriented along the polarization vector, while the $3p_x$ orbital is oriented in the perpendicular direction. The results we obtain for the $3p_x$ initial state are shown in Fig. 10. One can see that the correlation pattern we obtain in this case is qualitatively similar to the case of the $3p_z$ initial state of argon shown in Fig. 5.



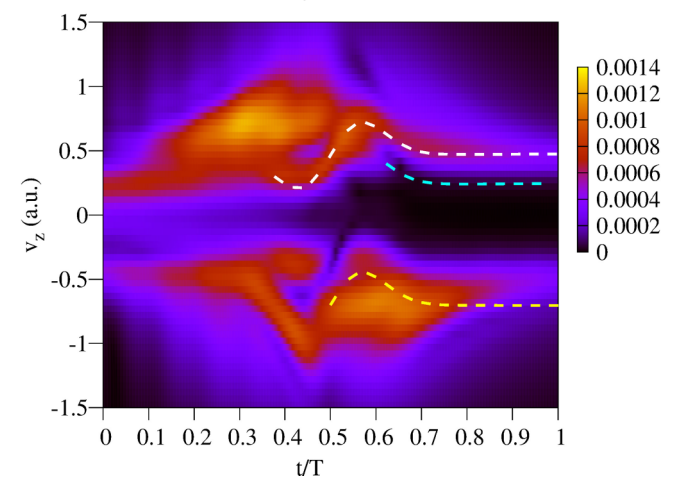


FIG. 10. Absolute values of the correlation function for electron velocity for argon atom for the $3p_x$ initial state. Dashed lines in the plots show the CTMC trajectories for the electrons launched at the local maxima of the electric field at t = 0.377 T (white), t = 0.5 T (yellow), and t = 0.623 T (cyan), respectively.

VI. SUMMARY AND CONCLUSION

In the present work, we investigate the process of nonadiabatic tunneling from an atom subjected to a very short and intense laser pulse. Our results are based on the correlation analysis of tunneling ionization in the model Yukawa and the hydrogen, helium, and argon atoms. We analyze the correlation function which links the two observables: the longitudinal electron velocity and the appearance of a photoelectron in the continuum at the end of the laser pulse. This approach allows us to single out the ionized wave packet from the total wave function describing evolution of the system and to visualize evolution of the photoelectron longitudinal velocity in real time as the ionization process develops. For a model atom bound by the Yukawa potential we find, in agreement with the basic premises of the SMM model, that the photoelectron emerges from the tunnel with the zero velocity. For the H, He, and Ar atoms bound by a Coulomb potential, the initial velocity at the tunnel is clearly nonzero.

We supplement our correlation analysis with an analysis of the sub-barrier electron motion relying on the quantum orbits method. Results produced by the two methods are in good agreement. This study allowed us to attribute the nonzero longitudinal velocity at the tunnel exit to the long-range Coulomb tail of the asymptotic ionic potential which is absent in the case of the model Yukawa atom.

ACKNOWLEDGMENTS

This work was supported by the Institute for Basic Science Grant (No. IBS-R012-D1) and the National Research Foundation of Korea (NRF), Grant funded by the Korea government (MIST) Grants (No. 2022R1A2C3006025) and (No. RS-2023-00218180). Work performed by A.S. and A.S.L. was supported by NSF Investigator-Initiated Research Grant,

Award No. 2208040. Computational work for this research were performed on the IBS Supercomputer Aleph in the IBS

Research Solution Center and the NCI Australia Supercomputer Facility.

- [1] J. Li, J. Lu, A. Chew, S. Han, J. Li, Y. Wu, H. Wang, S. Ghimire, and Z. Chang, Attosecond science based on high harmonic generation from gases and solids, Nat. Commun. 11, 2748 (2020).
- [2] C. F. de Morisson Faria and A. S. Maxwell, It is all about phases: Ultrafast holographic photoelectron imaging, Rep. Prog. Phys. 83, 034401 (2020).
- [3] T. Nubbemeyer, K. Gorling, A. Saenz, U. Eichmann, and W. Sandner, Strong-field tunneling without ionization, Phys. Rev. Lett. **101**, 233001 (2008).
- [4] L. V. Keldysh, Ionization in the field of a strong electromagnetic wave, Sov. Phys. JETP 20, 1307 (1965).
- [5] M. Lewenstein, P. Balcou, M. Y. Ivanov, A. L'Huillier, and P. B. Corkum, Theory of high-harmonic generation by lowfrequency laser fields, Phys. Rev. A 49, 2117 (1994).
- [6] P. B. Corkum, Plasma perspective on strong field multiphoton ionization, Phys. Rev. Lett. 71, 1994 (1993).
- [7] A. M. Perelomov, V. S. Popov, and M. V. Terentiev, Ionization of atoms in an alternating electric field, Sov. Phys. JETP 23, 924 (1966).
- [8] G. L. Yudin and M. Y. Ivanov, Nonadiabatic tunnel ionization: Looking inside a laser cycle, Phys. Rev. A 64, 013409 (2001).
- [9] M. Y. Ivanov, M. Spanner, and O. Smirnova, Anatomy of strong field ionization, J. Mod. Opt. 52, 165 (2005).
- [10] P. Eckle, M. Smolarski, P. Schlup, J. Biegert, A. Staudte, M. Schöffler, H. G. Muller, R. Dörner, and U. Keller, Attosecond angular streaking, Nat. Phys. 4, 565 (2008).
- [11] P. Eckle, A. N. Pfeiffer, C. Cirelli, A. Staudte, R. Dörner, H. G. Muller, M. Büttiker, and U. Keller, Attosecond Ionization and Tunneling Delay Time Measurements in Helium, Science 322, 1525 (2008).
- [12] A. N. Pfeiffer, C. Cirelli, M. Smolarski, D. Dimitrovski, M. Abu-Samha, L. B. Madsen, and U. Keller, Attoclock reveals natural coordinates of the laser-induced tunnelling current flow in atoms, Nat. Phys. 8, 76 (2012).
- [13] R. Boge, C. Cirelli, A. S. Landsman, S. Heuser, A. Ludwig, J. Maurer, M. Weger, L. Gallmann, and U. Keller, Probing nonadiabatic effects in strong-field tunnel Ionization, Phys. Rev. Lett. 111, 103003 (2013).
- [14] I. A. Ivanov and A. S. Kheifets, Strong-field ionization of He by elliptically polarized light in attoclock configuration, Phys. Rev. A **89**, 021402(R) (2014).
- [15] C. Hofmann, A. S. Landsman, and U. Keller, Attoclock revisited on electron tunnelling time, J. Mod. Opt. 66, 1052 (2019).
- [16] A. S. Kheifets, The attoclock and the tunneling time debate, J. Phys. B **53**, 072001 (2020).
- [17] U. S. Sainadh, R. T. Sang, and I. V. Litvinyuk, Attoclock and the quest for tunnelling time in strong-field physics, J. Phys. Photon. **2**, 042002 (2020).
- [18] C. Hofmann, A. Bray, W. Koch, H. Ni, and N. I. Shvetsov-Shilovski, Quantum battles in attoscience: Tunnelling, Eur. Phys. J. D **75**, 208 (2021).
- [19] P. Ge, M. Han, Y. Deng, Q. Gong, and Y. Liu, Universal description of the attoclock with two-color corotating circular fields, Phys. Rev. Lett. **122**, 013201 (2019).

- [20] S. Brennecke, S. Eckart, and M. Lein, Attoclock with bicircular laser fields as a probe of velocity-dependent tunnel-exit positions, J. Phys. B 54, 164001 (2021).
- [21] X. Sun, M. Li, J. Yu, Y. Deng, Q. Gong, and Y. Liu, Calibration of the initial longitudinal momentum spread of tunneling ionization, Phys. Rev. A 89, 045402 (2014).
- [22] M. Han, M. Li, M.-M. Liu, and Y. Liu, Tunneling wave packets of atoms from intense elliptically polarized fields in natural geometry, Phys. Rev. A 95, 023406 (2017).
- [23] M. Li, M.-M. Liu, J.-W. Geng, M. Han, X. Sun, Y. Shao, Y. Deng, C. Wu, L.-Y. Peng, Q. Gong *et al.*, Experimental verification of the nonadiabatic effect in strong-field ionization with elliptical polarization, Phys. Rev. A 95, 053425 (2017).
- [24] S. Eckart, K. Fehre, N. Eicke, A. Hartung, J. Rist, D. Trabert, N. Strenger, A. Pier, L. P. H. Schmidt, T. Jahnke *et al.*, Direct experimental access to the nonadiabatic initial momentum offset upon tunnel ionization, Phys. Rev. Lett. 121, 163202 (2018).
- [25] A. Geyer, D. Trabert, M. Hofmann, N. Anders, M. S. Schöffler, L. P. H. Schmidt, T. Jahnke, M. Kunitski, R. Dörner, and S. Eckart, Experimental fingerprint of the electron's longitudinal momentum at the tunnel exit in strong field ionization, Phys. Rev. Res. 5, 033094 (2023).
- [26] M. Li, H. Xie, W. Cao, S. Luo, J. Tan, Y. Feng, B. Du, W. Zhang, Y. Li, Q. Zhang *et al.*, Photoelectron holographic interferometry to probe the longitudinal momentum offset at the tunnel exit, Phys. Rev. Lett. 122, 183202 (2019).
- [27] C. Hofmann, A. Landsman, C. Cirelli, A. Pfeiffer, and U. Keller, Comparison of different approaches to the longitudinal momentum spread after tunnel ionization, J. Phys. B 46, 125601 (2013).
- [28] A. S. Landsman and U. Keller, Attosecond science and the tunnelling time problem, Phys. Rep. 547, 1 (2015).
- [29] N. I. Shvetsov-Shilovski, D. Dimitrovski, and L. B. Madsen, Ionization in elliptically polarized pulses: Multielectron polarization effects and asymmetry of photoelectron momentum distributions, Phys. Rev. A 85, 023428 (2012).
- [30] J. Tian, X. Wang, and J. H. Eberly, Numerical detector theory for the longitudinal momentum distribution of the electron in strong field ionization, Phys. Rev. Lett. 118, 213201 (2017).
- [31] R. Xu, T. Li, and X. Wang, Longitudinal momentum of the electron at the tunneling exit, Phys. Rev. A 98, 053435 (2018).
- [32] S. Luo, M. Li, W. Xie, K. Liu, Y. Feng, B. Du, Y. Zhou, and P. Lu, Exit momentum and instantaneous ionization rate of nonadiabatic tunneling ionization in elliptically polarized laser fields, Phys. Rev. A 99, 053422 (2019).
- [33] Z. Xiao, W. Quan, S. Yu, X. Lai, X. Liu, Z. Wei, and J. Chen, Nonadiabatic strong field ionization of noble gas atoms in elliptically polarized laser pulses, Opt. Express 30, 14873 (2022).
- [34] I. Ivanov and K. T. Kim, Analysis of correlations in strong field ionization, J. Phys. B 55, 055001 (2022).
- [35] I. Ivanov and K. T. Kim, Joint probability calculation of the lateral velocity distribution in strong field ionization process, Sci. Rep. 12, 19533 (2022).

- [36] I. A. Ivanov, A. S. Kheifets, and K. T. Kim, Correlation analysis of frustrated tunneling ionization, Phys. Rev. A 107, 043106 (2023).
- [37] I. A. Ivanov, A. S. Kheifets, and K. T. Kim, Tracking quantum-cloud expansion in tunneling ionization, Phys. Rev. A **108**, 053108 (2023).
- [38] F. H. M. Faisal, Multiple absorption of laser photons by atoms, J. Phys. B 6, L89 (1973).
- [39] H. R. Reiss, Effect of an intense electromagnetic field on a weakly bound system, Phys. Rev. A 22, 1786 (1980).
- [40] V. S. Popov, Tunnel and multiphoton ionization of atoms and ions in a strong laser field, Phys. Usp. 47, 855 (2004).
- [41] A. Rudenko, K. Zrost, T. Ergler, A. B. Voitkiv, B. Najjari, V. L. B. de Jesus, B. Feuerstein, C. D. Schröter, R. Moshammer, and J. Ullrich, Coulomb singularity in the transverse momentum distribution for strong-field single ionization, J. Phys. B 38, L191 (2005).
- [42] N. B. Delone and V. P. Krainov, Energy and angular electron spectra for the tunnel ionization of atoms by strong low-frequency radiation, J. Opt. Soc. Am. B 8, 1207 (1991).
- [43] S. V. Popruzhenko, Keldysh theory of strong field ionization: History, applications, difficulties and perspectives, J. Phys. B 47, 204001 (2014).
- [44] A. M. Steinberg, Conditional probabilities in quantum theory and the tunneling-time controversy, Phys. Rev. A 52, 32 (1995).
- [45] D. Sokolovski and J. N. L. Connor, Negative probability and the distributions of dwell, transmission, and reflection times for quantum tunneling, Phys. Rev. A 44, 1500 (1991).
- [46] D. J. Miller, Conditional probabilities in quantum mechanics from a time-symmetric formulation, Nuovo Cimento B 112, 1577 (1997).

- [47] P. Lambropoulos and D. Petrosyan, *Fundamentals of Quantum Optics and Quantum Information* (Springer-Verlag, Berlin, 2007).
- [48] I. A. Ivanov, Evolution of the transverse photoelectronmomentum distribution for atomic ionization driven by a laser pulse with varying ellipticity, Phys. Rev. A **90**, 013418 (2014).
- [49] I. A. Ivanov and A. S. Kheifets, Time delay in atomic photoionization with circularly polarized light, Phys. Rev. A 87, 033407 (2013).
- [50] I. A. Ivanov, J. Dubau, and K. T. Kim, Nondipole effects in strong-field ionization, Phys. Rev. A 94, 033405 (2016).
- [51] L. Torlina, F. Morales, J. Kaushal, I. Ivanov, A. Kheifets, A. Zielinski, A. Scrinzi, H. G. Muller, S. Sukiasyan, M. Ivanov et al., Interpreting attoclock measurements of tunnelling times, Nat. Phys. 11, 503 (2015).
- [52] H. Ni, U. Saalmann, and J.-M. Rost, Tunneling ionization time resolved by backpropagation, Phys. Rev. Lett. 117, 023002 (2016).
- [53] A. W. Bray, S. Eckart, and A. S. Kheifets, Keldysh-Rutherford model for the attoclock, Phys. Rev. Lett. 121, 123201 (2018).
- [54] V. V. Serov, A. W. Bray, and A. S. Kheifets, Numerical attoclock on atomic and molecular hydrogen, Phys. Rev. A 99, 063428 (2019).
- [55] A. Sarsa, F. J. Gálvez, and E. Buendia, A parametrized optimized effective potential for atoms, J. Phys. B 36, 4393 (2003).
- [56] X.-Y. Lai, C. Poli, H. Schomerus, and C. F. d. M. Faria, Influence of the Coulomb potential on above-threshold ionization: A quantum-orbit analysis beyond the strong-field approximation, Phys. Rev. A 92, 043407 (2015).
- [57] N. I. Shvetsov-Shilovski, Semiclassical two-step model for ionization by a strong laser pulse: further developments and applications, Eur. Phys. J. D 75, 130 (2021).